Tingting Ye
Department of Mechanical Engineering,
Wuhan University,
Wuhan 430072, China
e-mail: tilda_ye@whu.edu.cn

Jie Ling[1]
Department of Mechanical Engineering,
Wuhan University,
Wuhan 430072, China
e-mail: jamesling@whu.edu.cn

Xi Kang
Department of Biomedical Engineering,
National University of Singapore,
Singapore 117608
e-mail: xi.kang@nus.edu.sg

Zhao Feng
Department of Mechanical Engineering,
Wuhan University,
Wuhan 430072, China
e-mail: fengzhaozhao7@whu.edu.cn

Xiaohui Xiao
Department of Mechanical Engineering,
Wuhan University,
Wuhan 430072, China
e-mail: xhxiao@whu.edu.cn

A Novel Two-Stage Constant Force Compliant Micrograpper

The manipulating objects of the micron scale are easily damaged, hence the microgrippers, the key components in micro manipulating systems, demand precise force control, plus miniaturized size. Consequently, the constant force microgrippers, generally lack the ability to fit different sizes. To avoid the overload damage, apply multi-size microparts and simplify the control method, a novel two-stage compliant constant force microgripper is proposed in this paper. Based on the negative stiffness effect, this gripper is connected in parallel with a two-stage negative stiffness module and a positive stiffness module. Then, the elliptic integral method and the pseudo-rigid-body method are both employed to derive the kinetostatic and dynamic performances. Finally, the analytical results are validated. It is observed that two-stage constant forces of 1.33 N in 305.6 μm and 1.11 N in 330.8 μm are acquired.
[DOI: 10.1115/1.4048217]

Keywords: microgripper, overloading protection, compliant mechanisms, negative stiffness, micro and nano systems

1 Introduction

During the last decades, rapid development has been witnessed in the field of robotic manipulation. To deal with the trend toward miniaturized target objects, automated pick-and-place operation with high precision attracts many efforts to develop efficient micromanipulators [1–5]. Due to the merits of the flexibility to different shaped objects, fast responses with ultrahigh accuracy and low cost, piezoelectric actuated microgrippers have been widely used in various applications, including but not limiting to aerospace [6], biomedical engineering [7,8] and micro electromechanical systems [9–12]. In general, microgrippers can be roughly divided into two categories: (i) rigid type and (ii) compliant type. Compared with the former, compliant grippers have the advantages of no wear, no backlash, no friction, no assembly, and no lubrication [13]. On the other hand, the integrated structure that reduces the overall size [14] is also one main reason why compliant grippers are much more welcome in micromanipulations.

A challenge of compliant grippers for micromanipulations lies in that target objects on the micron scale are quite sensitive to changes in gripping force due to scale effect and adhesion effect [15]. It is extremely important to control the force accurately in gripping stroke in case of damage to clamping objects. For some instances, (i) the assembly of optical fibers requires gripping stroke of 100 μm and gripping force about 300 mN [16]; (ii) the microinjection of a custom-built cell requires gripping force less than 71 mN after 4.4 mm [17], etc. Consequently, two ways to realize precise grasp while maintaining objects undamaged are developed. One method is installing the displacement and force sensors. By this, the gripper can detect and control the contact force through well-designed controllers [18]. However, it will meanwhile increase the overall size, improve the structure complexity, and bring signal processing burden. Another method is designing constant force mechanisms (CFMs). A gripper can provide near-constant force in particular gripping stoke through well-designed CFMs. This will protect the object from overload without additional sensors or complicated force control algorithms [19]. Hence, the grippers based on CFMs have broader applications and preferable prospects.

Nowadays, abundant studies on single-stage constant force microgrippers have emerged which can be classified in terms of parallel and series. For the parallel type, a negative stiffness module and a positive stiffness module can be connected in parallel to acquire a zero stiffness in a special stroke. Parallel microgrippers with a CFM have been proposed in Refs. [20–23]. In these prototypes, an inclined beam and a straight beam are fixed and guided in the same end. This design can protect micro objects from overloading. However, they can merely be applied to clamp a particular kind of objects in a short range. Moreover, additional stress for parallel structure and large size of constant force module also restrict the applications of this type. For the series type, the deformations are delivered from one module to another. Series microgrippers with CFMs are realized by connecting single inclined or straight beams end to end in Refs. [17,24]. Another series type is using beams with particular continuous curves as in Refs. [25,26]. The curve structure creates less additional stress when clamping objects compared with parallel types. However, the complicated curve increases the complexity of fabrication and maintainability. On top of that, both the parallel and series microgrippers with single-stage constant force are not applicable for grasping multi-size objects without damage as constant contact force within only one specific stroke can be guaranteed. To implement complicated operations such as microassembly of multi-size micro-electro-mechanical system (MEMS) parts, microgrippers with more than one constant force stage need to be investigated.

Some multi-stage CFMs are proposed in Refs. [27–33], such as adjustable and unadjustable multi-stage constant force mechanisms.

[1]Corresponding author.

Contributed by Mechanisms and Robotics Committee of ASME for publication in the Journal of Mechanical Design. Manuscript received February 18, 2020; final manuscript received July 21, 2020; published online October 28, 2020. Assoc. Editor: Hai-Jun Su.

The constant force can be adjusted through a changeable preloading displacement so that multi-stage constant force can be indirectly realized in Refs. [27–29]. By assembly or disassembly of the constant force module, adjustable CFMs are obtained in Refs. [30,31]. Although the designs in Refs. [27–31] have simple structures and large strokes, the operating efficiency is low and the entire dimension is relatively large, which cannot be applied into microgrippers. A module that is composed of fixed-guided beams with multi negative stiffness in nonoverlapping ranges connected with a positive stiffness module has been developed in Refs. [32,33] to synthesize unadjustable multi-stage CFMs. This structure has better switching continuity, efficiency, flexibility, and integrability than those in Refs. [27–31]. Nevertheless, kinetics/dynamics modeling and analyzing are difficult because of the operating principle and complicated structure. Hence, the development of unadjustable multi-stage constant force microgrippers is hampered by optimization of parameters design (i.e., the particular values of stiffness and critical positions of buckling) which can be derived by the analytical model.

With respect to the modeling method for microgrippers with compliant mechanisms, a large amount of methods are developed in Refs. [34–44]. Given that the chain algorithm, the finite element method, etc. in Refs. [34–38] possess complexity, immaturity, and high sensitivity of loading conditions, two main methods can be considered, including the pseudo-rigid-body method (PRBM) [39–41] and elliptic integral method (EIM) [42–44]. PRBM is effective by approximating a flexure to a rigid-body mechanism. However, this deteriorates the accuracy of transformation so that it cannot be directly used for large deformation. EIM based on Bernoulli Euler beam theory is a classical mathematical tool to deal with large deformation whose characteristics are predicted accurately on account of differential equations. Compared to PRBM, EIM performs better in accuracy but brings great difficulties to design with its computing complexity, especially in thin beams with complex shapes.

The demands for conducting overload protection, enhancing multi-size adaptability, and improving control simplicity need to be taken into consideration comprehensively in the mechanism design. Motivated by the aforementioned essential issues, this paper aims to devise a two-stage constant force microgripper (TSCFM) in which the constant force switching is carried out continuously during the gripping process for overloading protection. In this work, a two-stage CFM is realized through combing a two-stage negative stiffness module with a linear positive stiffness module through parallel connection. Compared with the constant force designs in Refs. [20–33], the proposed TSCFM has a series of advantages as follows: (i) the output performance of the two-stage constant force make the TSCFM more suitable for the micro-assembly of multiple parts than the single-stage ones in Refs. [20–26]; (ii) the continuous switching between two-stage constant forces in the gripping process makes microoperations more efficient than Refs. [27–31]; and (iii) the integrated structure contributes to the miniaturization of the overall size and flexibility of operation as well. Considering inherent bistability and nonlinearity, the kineto-static model of the negative stiffness module is firstly established using EIM. The kinetic and static model of the leverage mechanism is then established by PRBM. On the basis of these, the kinetostatic and dynamic models of TSCFM are established by the hybrid method of EIM and PRBM. Hereto, structure parameters can be optimized using the established model of the TSCFM. The main contributions of this paper are as follows: (i) a two-stage CFM by means of the parallel connection between multi-stage negative and positive stiffness modules is developed to adapt to manipulations of objects of various sizes and (ii) a hybrid EIM and PRBM model is established for the proposed TSCFM to optimize the structure parameters.

The remainder of this paper is organized as follows. The design principle and the proposed mechanism of the gripper in introduced in Sec. 2. Structure parameters and analytical results are derived in Sec. 3 based on kinetostatic and dynamic modeling by EIM and PRBM. The performance is verified through simulations using a finite element method (FEM) in Sec. 4. Finally, Sec. 5 concludes this paper.

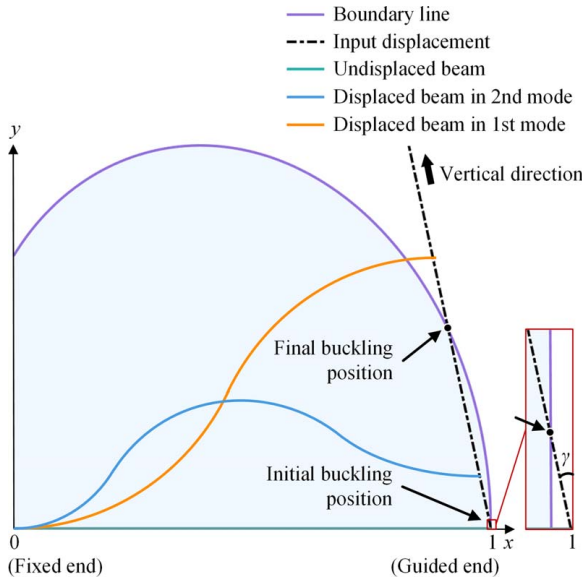

Fig. 1 The transition of buckling modes during the deformation of fixed-guided beam

2 Design of Two-Stage Constant Force Microgripper

2.1 Working Principle. Conventional CFMs are connected by rods, cams, springs, and so on through rigid hinges, whereas TSCFM proposed in this paper is composed of flexure beams, rigid rods, and compliant hinges based on the negative stiffness effect. The bistable state is shown during buckling deformation of fixed-guided beams with inclined angles, called the first buckled mode and the second buckled mode. The transition of buckled modes correspond to the change of stiffness as shown in Fig. 1, where the x-axis refers to the normalized displacement in the x-direction, the y-axis refers to the normalized displacement in the y-direction, boundary line separates the first and second buckled modes and γ refers to the initial angle of the fixed-guided beam.

Determined by the position of the guided end, the first and the second buckled modes correspond to the white and blue areas, respectively. The changing process of stiffness is as follows. Initially, the beam with the initial angle of γ receives a vertical

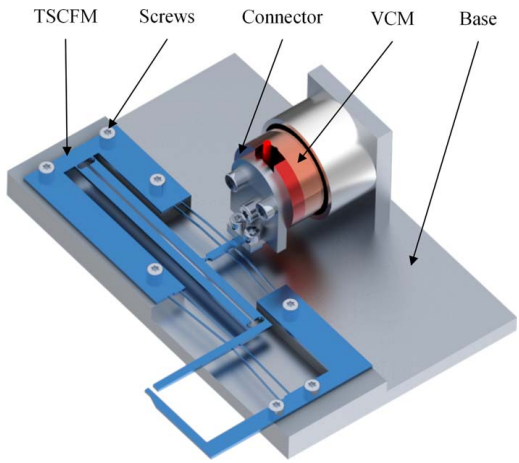

Fig. 2 The proposed two-stage constant force microgripper (TSCFM)

displacement, increases the stored energy, and shows positive stiffness until the deformation reaches the boundary line the first time. This critical buckling position is called the initial one. And then, negative stiffness appears with the decrease in energy until the deformation reaches the boundary line the second time. This critical buckling position is called the final one. After that, the beam starts storing energy and shows positive stiffness again. Only if the negative stiffness beams are connected with the positive stiffness mechanism, the zero-stiffness mechanism (i.e., CFM) will be derived.

Based on negative stiffness effect, the proposed TSCFM is shown in Fig. 2, where the TSCFM is actuated by a voice coil motor (VCM). The design objective consists in performing two-stage constant force in two strokes continuously, which could have been ideally realized by the parallel connection of bistable beam module (BBM) 1 and BBM 2. However, it stands for the supremely harsh requirement for structure parameters since the stiffness performed in two strokes may be unequal or nonzero commonly. As a consequence, a more realizable design scheme is proposed below.

As demonstrated in Fig. 3, BBM 1 and BBM 2 are connected in parallel to achieve parallel connection I whose force–displacement curve requires a same negative stiffness in two nonoverlapping stokes (s_1, e_1) and (s_2, e_2). Then parallel connection I and positive stiffness module compose parallel connection II which shows zero stiffness in these strokes. Hence, (s_1, e_1) and (s_2, e_2) are the two constant force strokes; (0, e_2) is the effective stroke where it is no danger of overload damage to the gripping objects in structure sizes below e_2.

The mechanism design puts forward the extremely high request to the stiffness performances of which the relationship is exhibited as

$$K_{I1} = K_{I2} = -K\,p \tag{1}$$

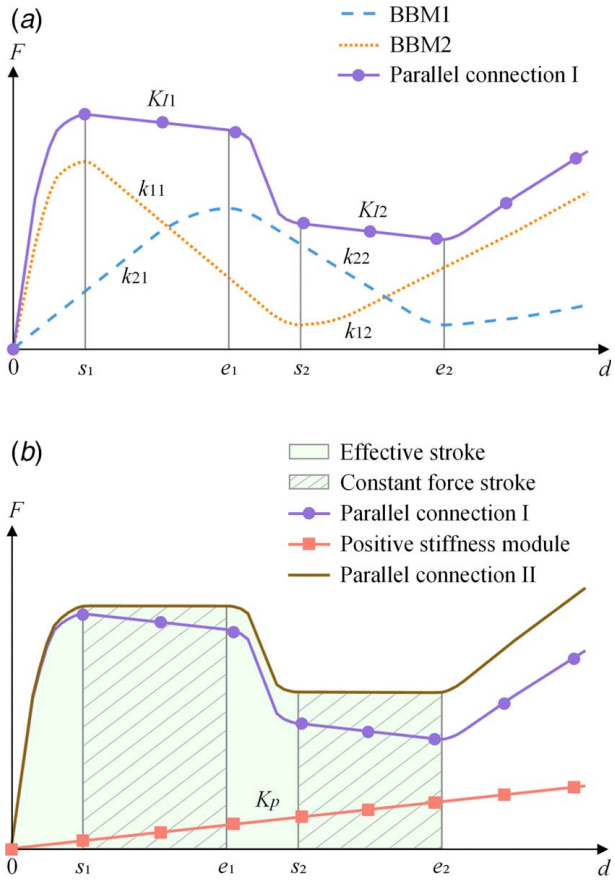

Fig. 3 Force to displacement curves of TSCFM: (*a*) two-stage negative stiffness and (*b*) two-stage zero stiffness

where

$$K_{I1} = k_{11} + k_{21}$$
$$K_{I2} = k_{12} + k_{22} \tag{2}$$

K_{I1}, k_{11}, and k_{21} are the stiffnesses of parallel connection I, BBM 2, and BBM 1 in (s_1, e_1); K_{I2}, k_{12}, and k_{22} are the stiffnesses of parallel connection I, BBM 2, and BBM 1 in (s_2, e_2); and K_p is the linear stiffness of the positive stiffness module.

Parallel connection II shows zero stiffness in two nonoverlapping strokes, which means two-stage constant force in a continuous gripping process is achieved.

2.2 Mechanism Design. As shown in Fig. 4, the TSCFM is composed of BBM 1 (beam 1(a), beam 1(b), and shuttle 1), BBM 2 (beam 2(a), beam 2(b), and shuttle 2), leverages, flexure hinges, etc. In order to guarantee guidance and required stiffness characteristics at the same time, BBMs 1 and 2 are both composed of two layers of fixed-guided beams symmetrically. The leverages connect BBM 1, BBM 2, and the base by notched circular flexure hinges whose flexure parts are so short and thin that the elastic restoring force is very small during deformation. Furthermore, two leverages of the same length and shuttles form a parallelogram mechanism to get the flat shift of the output end. Therefore, the jaws can clamp parallelly rather than rotationally to ensure better stability and adaptability, which inevitably sacrifices certain amplifying ratio.

Besides, the parallelogram mechanism brings inevitable parasitic motion. Shuttle 2 will have a small bias due to the constraints of the fixed-guided beams. We adopt the symmetrical arrangement with two layers to suppress it.

It is necessarily acknowledged that the input end and output end are, respectively, shuttle 1 and shuttle 2. In the whole effective stroke where the crisp objects have no risk of overloading damage, leverages have the ability not only to amplify the input displacement of shuttle 1 but also to serve as a positive stiffness module. Although the leverages bring extra displacement in the x-axis inevitably, the parallelogram mechanism still plays an important role because the amplified displacement of shuttle 1 is the precondition for design. With an appropriate amplifying ratio, the initial and final buckling positions of BBM 1 are e_1 and e_2 of the output displacement; the initial and final buckling positions of BBM 2 are s_1 and s_2 of the output displacement; their relations need to be: $0 < s_1 < e_1 < s_2 < e_2$. Since force is inversely proportional to displacement in (e_1, s_2), (s_1, e_1) and (s_2, e_2) as two constant force ranges show two different values of the force.

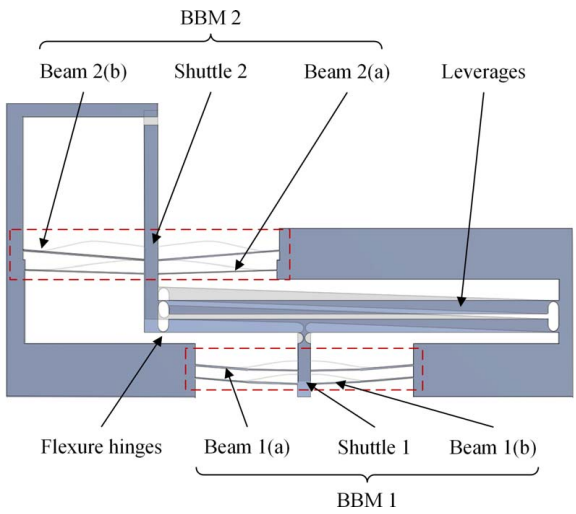

Fig. 4 The top view of TSCFM

3 Modeling and Analysis

In this section, the elliptic integral method and the pseudo-rigid-body method are both introduced. Considering the bistability and nonlinearity of fixed-guided beams, the elliptic integral method is employed to deal with large deformation for solving output force performances. The pseudo-rigid-body method is utilized in kinematic and dynamic modeling, because the positions of the "rigid" parts (i.e. the shuttles, the levers, etc.) are the main concerns in kinematic modeling, and their mass in the dynamic modeling is much greater than that of the flexible parts.

3.1 Kinetostatic Modeling

3.1.1 Kinetostatic Model of the Fixed-Guided Beam. An analytical model is established to derive the vertical force reaction in the guided end corresponding to input displacement. In that case, it is divided into the bending model and deflection model.

A. Bending model

The length L of a fixed-guided beam is assumed to be invariable in the bending model. According to the Bernoulli Euler beam theory, the moment in the beam at a random point P as shown in Fig. 5 can be expressed as

$$EI\frac{d\theta}{ds} = M - Fx\sin\beta + Fy\cos\beta \tag{3}$$

where E is the elasticity modulus of the material; I is the inertia moment of the bistable beam; θ is the rotational angle of the point P on the beam; x and y are the horizontal and vertical displacement of this point; F is the force reaction on the guided end, β is the angle between F and the x-axis.

For uniform expression, dx and dy are expressed as

$$\begin{aligned} dx &= ds\cos\theta \\ dy &= ds\sin\theta \end{aligned} \tag{4}$$

After the derivative and integration transformation, Eq. (3) can be expressed as

$$EI\left(\frac{d\theta}{ds}\right)^2 = -2F\cos(\theta-\beta) + 2R \tag{5}$$

where R is a constant produced by the integral transformation.

According to geometric relation conversion, it can be sorted out as

$$\begin{aligned} L &= \int_0^L ds \\ b_x &= \int_0^L \cos\theta\, ds \\ b_y &= \int_0^L \sin\theta\, ds \end{aligned} \tag{6}$$

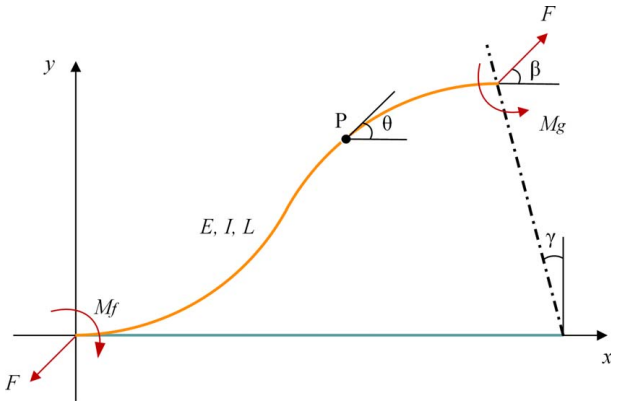

Fig. 5 Variables diagram of fixed-guided beam

where b_x and b_y are the horizontal and vertical coordinates of the guided end due to bending.

Substituting Eq. (5) into Eq. (6), length L with respect to θ is

$$L = \int\sqrt{\frac{EI}{-2F\cos(\theta-\beta)+2R}}\,d\theta \tag{7}$$

where θ does not change monotonically from the fixed end to the guided end. The mapping from θ to deformation being hardly established, the incomplete elliptic integrals of the first and second kind are involved as

$$\begin{aligned} F(h,\varphi) &= \int_0^{\varphi}\frac{d\delta}{\sqrt{1-h^2\sin^2\delta}} \\ E(h,\varphi) &= \int_0^{\varphi}\sqrt{1-h^2\sin^2\delta}\,d\delta \end{aligned} \tag{8}$$

where

$$\begin{aligned} h &= \sqrt{\frac{R+F}{2F}} \\ \varphi &= \arcsin\left(\frac{1}{h}\cos\frac{(\theta-\beta)}{2}\right) \end{aligned} \tag{9}$$

The value of φ ranges from φ_1 to φ_2. It can be understood as a variable that changes monotonically from the fixed end to guided end. It is observed that the inflection point of the beam appears once φ is an odd multiple of $\pi/2$.

The trigonometric substitution of above formulas gives

$$d\theta = \pm\frac{2h\cos\varphi}{\sqrt{1-h^2\sin^2\varphi}}\,d\varphi \tag{10}$$

Then, whether it is positive or negative should be discussed in two modes as Fig. 6.

When φ ranges from φ_1 to $\pi/2$ in the first mode, $\cos\varphi$ and $d\theta/d\varphi$ are both positive; and when it ranges from $\pi/2$ to φ_2, they are both negative. Similarly, these values in the second mode can be analyzed, so the result is

$$d\theta = \frac{2h\cos\varphi}{\sqrt{1-h^2\sin^2\varphi}}\,d\varphi \tag{11}$$

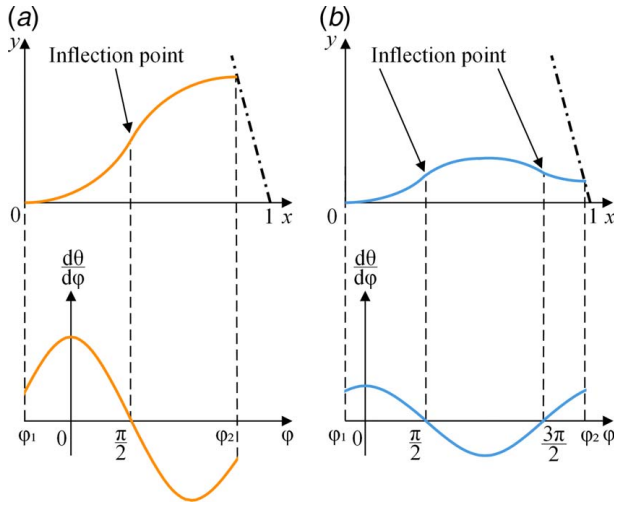

Fig. 6 The derivative of θ with respect to φ in: (*a*) first mode and (*b*) second mode

Therefore, the x- and y-coordinates of the guided end due to bending are

$$b_x = \sqrt{\frac{EIL^2}{F}}\left[\cos\beta\left(\widehat{F} - 2\widehat{E}\right) - 2h\sin\beta\left(\cos\varphi_2 - \cos\varphi_1\right)\right]$$
$$b_y = \sqrt{\frac{EIL^2}{F}}\left[\sin\beta\left(\widehat{F} - 2\widehat{E}\right) - 2h\cos\beta\left(\cos\varphi_2 - \cos\varphi_1\right)\right] \tag{12}$$

where

$$\widehat{E} = E(h, \varphi_2) - E(h, \varphi_1)$$
$$\widehat{F} = F(h, \varphi_2) - F(h, \varphi_1) \tag{13}$$

B. Deflection model

Since the boundary conditions cannot be satisfied only by the bending model, the deformation of axial deflection must be considered. Though often used for small deformation, Hooke's Law can be adapted to this condition that the deformation due to bending is much larger than deflection. The axial strain of the fixed-guided beam is

$$\varepsilon = \frac{F\cos(\theta - \beta)}{EA} \tag{14}$$

where A is the sectional area of the fixed-guided beam. In the same manner as the bending model, the normalized x- and y-displacements of the guided end due to axial deflection are

$$D_x = \sqrt{\frac{FI}{EA^2}}\int_{\varphi_1}^{\varphi_2}\left(2h^2\sin^2\varphi - 1\right)\cos\theta\, d\varphi$$
$$D_y = \sqrt{\frac{FI}{EA^2}}\int_{\varphi_1}^{\varphi_2}\left(2h^2\sin^2\varphi - 1\right)\sin\theta\, d\varphi \tag{15}$$

Finally, the x- and y-coordinates of the guided end are

$$l_x = b_x + D_x$$
$$l_y = b_y + D_y \tag{16}$$

C. The determination of boundary line

Additionally, it is necessary to draw a boundary line to ascertain the buckled modes previously. If the beam were in the first buckled mode, the relationship between φ_1 and φ_2 is as Eq. (17) according to boundary condition that θ of both ends is zero.

$$\varphi_1 + \varphi_2 = \pi \tag{17}$$

Otherwise, it gives

$$\varphi_2 - \varphi_1 = 2\pi \tag{18}$$

Obviously, the value of φ_1 is $-\pi/2$ when the guided end is on the boundary line. Combined with Eq. (9), the value of h with respect to β is as

$$h = -\cos\frac{\beta}{2} \tag{19}$$

where β corresponds to the angle between the line from the fixed end to a point on the boundary line and the x-axis, ranging from π to $3\pi/2$. The boundary line can be figured out by taking the directional angle of force reaction β as the independent variable and the position of the guided end as the dependent variable. If the actual coordinates of the guided end were below or above the boundary line, it is in the first buckled mode or second buckled mode separately.

D. The solution to output force performance

The computing method to solve analytical model is shown in Fig. 7.Given the input displacement d, then the actual coordinates

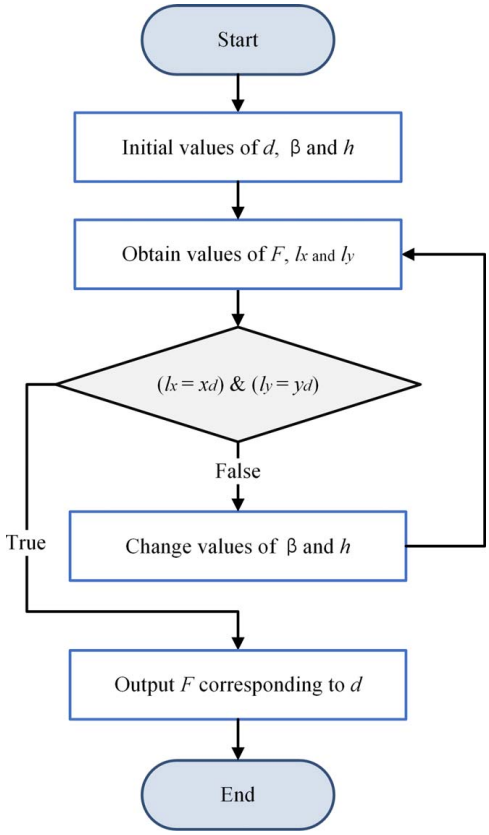

Fig. 7 The computing method of $F-d$ curve of the fixed-guided beam

of the guided end x_d and y_d can be figured out as

$$x_d = L - d\sin\gamma$$
$$y_d = d\cos\gamma \tag{20}$$

The theoretical coordinates l_x and l_y are available by adjusting the values of h and β until the theoretical coordinates coincide with the actual ones. If their values were equal, the force reaction corresponding to given variables may be expressed as

$$F = \frac{EI}{L^2}\left(\int_{\varphi_1}^{\varphi_2}\frac{d\varphi}{\sqrt{1 - h^2\sin^2\varphi}}\right)^2 \tag{21}$$

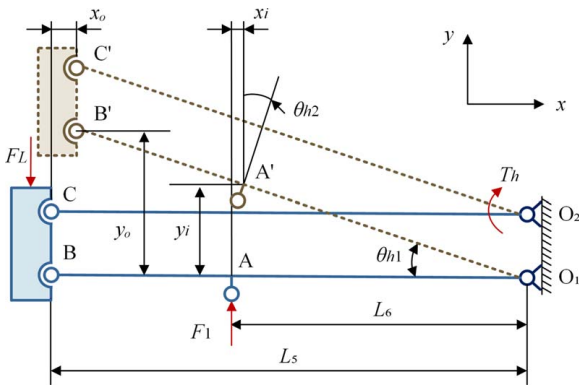

Fig. 8 The pseudo-rigid-body model of the leverage mechanism

3.1.2 Static Model of Leverage Mechanism. In order to make the combined modeling of TSCFM complete, the pseudo-rigid-body model of the leverage mechanism is shown in Fig. 8 where the energy relation can be expressed as

$$F_1 y_i + T_h \theta_{hi} = F_L y_o \tag{22}$$

where F_1 and F_L are the external forces on the leverage mechanism, T_h refers to the required moment for deformation of flexure hinges, θ_{hi} refers to the rotational angle of each hinge, and θ_{h2} is equal to θ_{h1}.

Due to the parallel relation between O_1B and O_2C, the removed BC (i.e., shuttle 2) is always perpendicular to the x-axis. Given that AA' is the input displacement, the amplifying ratio is

$$\alpha = \frac{d_o}{d_i} = \frac{y_o}{y_i} = \frac{L_5}{L_6} \tag{23}$$

In addition, the inevitable displacement of shuttle 2 in the x-axis is

$$x_o = L_5(1 - \cos\theta_{h1}) \tag{24}$$

The stiffness of single and double notched circular flexure hinges in Fig. 9 can be figured out as

$$k_{hi} = \sqrt{\frac{2nE^2 b^2 T_i^5}{81\pi^2 R_i}} \tag{25}$$

where n of single and double notched hinges are 1 and 2, respectively. It is easily seen that T_i plays a greater part for the value of stiffness than R_i. The rotational angle of leverage is small enough to estimate F_L as

$$F_L = \frac{F_1}{\alpha} + \frac{d_o}{L_5^2}\sum_{i=1}^{5} k_{hi} \tag{26}$$

Since BBM 1, BBM 2, and leverage mechanism are connected in parallel, the total force reaction of the combined model is

$$F_{out} = F_L + F_2 \tag{27}$$

where F_2 is the force reaction of BBM 2 whose values have been figured out by EIM.

3.2 Dynamic Modeling. The ratio of the shuttle mass over the beam mass determines whether the mass of fixed-guided beams significantly affects the natural frequencies. If the ratios are less than 10^6, the beam mass will be considered in dynamic modeling consequently. Moreover, the natural frequency decreases with increasing ratio, which should also be fully thought over in design.

To obtain the dynamic performance of the TSCFM, the equivalent stiffness K_e and mass M_e should be figured out since the governing differential equation is

$$M_e\ddot{x} + K_e\dot{x} = F_{out} \tag{28}$$

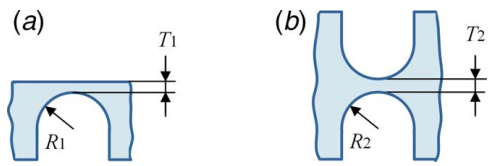

Fig. 9 The notched circular flexure hinges: (*a*) single notched hinge and (*b*) double notched hinge

Given the expression of output force $F_o ut$ as Eq. (27), the equivalent stiffness K_e is easily computed as

$$K_e = \lim_{t\to 0}\frac{F_{out}(t)}{d_o(t)} \tag{29}$$

The pseudo-rigid-body model of the TSCFM is shown in Fig. 10 by PRBM, where the parasitic motion of shuttle 2 produced by the lever is assumed not to exist.In fact, owing to the deformation of fixed-guided beams and flexure hinges, the overconstraint will not appear during the clamping process. Hence, the kinetic energy can be expressed as

$$\begin{aligned}\frac{1}{2}M_e\dot{d}_o^2 = \frac{1}{2}\Big(&\frac{1}{\alpha}m_{s1} + m_{s2} + \sum_{j=1}^{4}\frac{1-\xi}{2\alpha}m_{bj} \\ &+ \sum_{k=1}^{4}\frac{1-\xi}{2}m_{bk}\Big)\dot{d}_o^2 + \sum_{j=1}^{4}\frac{\xi}{2}J_{bj}\dot{\theta}_{bj}^2 \\ &+ \sum_{k=1}^{4}\frac{\xi}{2}J_{bk}\dot{\theta}_{bk}^2 + J_l\dot{\theta}_l^2 + \sum_{i=1}^{5}\frac{1}{2}J_{hi}\dot{\theta}_{hi}^2\end{aligned} \tag{30}$$

where $\dot{d}_o$ is the velocity of shuttle 2, m_{si} is the equivalent mass of ith shuttle, m_{bj} and J_{bj} are the mass and inertia moment of the jth fixed-guided beam of BBM 1, m_{bk} and J_{bk} are the mass and inertia moment of the kth fixed-guided beam of BBM 2, J_l is the inertia moment of leverage, J_{hi} is the inertia moment of the ith notched hinge, value of ξ is 0.85. Furthermore, it gives

$$\begin{aligned}\dot{\theta}_{bj} &= \frac{\dot{d}_o}{\alpha\xi L_{bj}}, \quad \dot{\theta}_{bk} = \frac{\dot{d}_o}{\xi L_{bk}} \\ \dot{\theta}_l &= \dot{\theta}_1 = \dot{\theta}_2 = \frac{\dot{d}_o}{L_5}\end{aligned} \tag{31}$$

Then, the natural frequency of the first mode under the analytical method may be expressed as

$$f_1 = \frac{1}{2\pi}\sqrt{\frac{K_e}{M_e}} \tag{32}$$

3.3 Sensitivity Analysis and Parameter Optimization. A series of F–d curves of the fixed-guided beams are exhibited as Fig. 11 to analyze the parametric sensitivity of output force performance, including length L, width t, thickness B, and initial angle γ. The significative properties contain the buckled ranges, the values of stiffness, etc. Then, each variable is changed with the constant

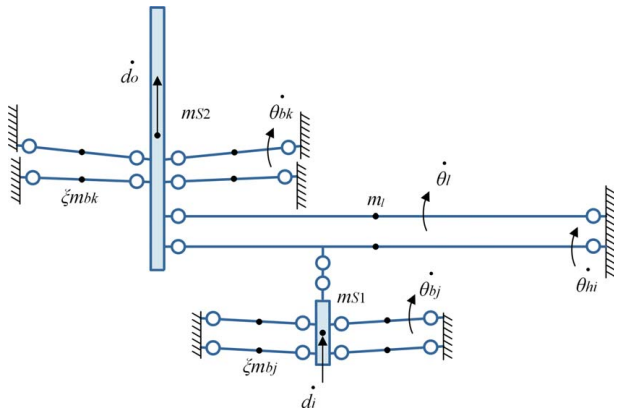

Fig. 10 The pseudo-rigid-body model of TSCFM

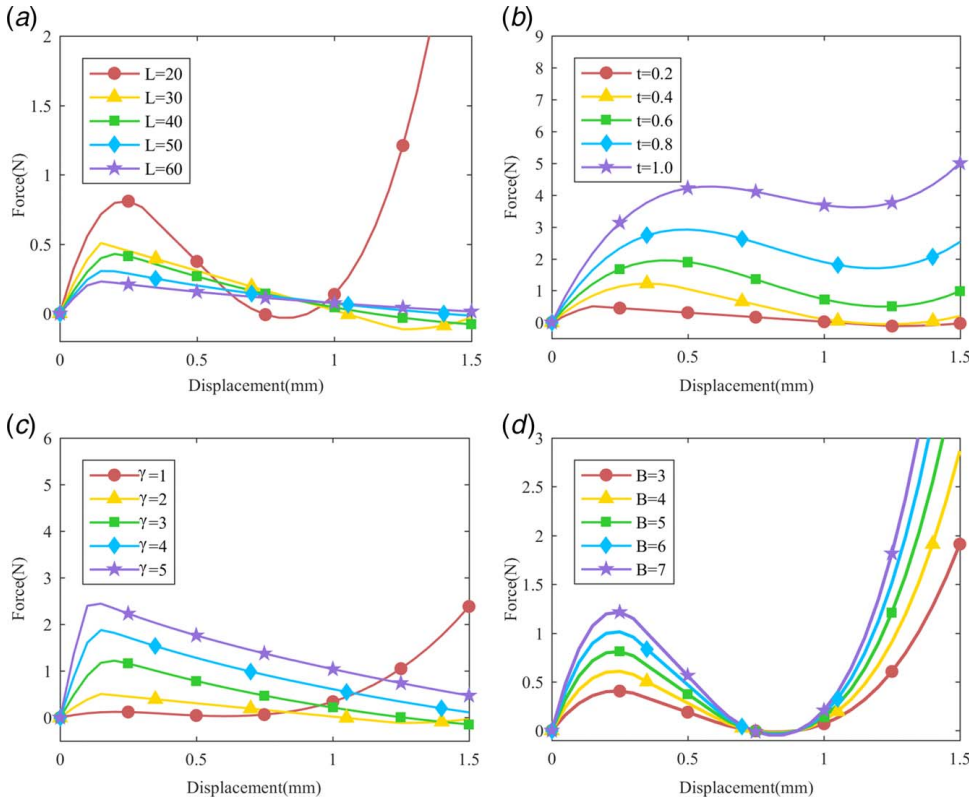

Fig. 11 The parametric sensitivity of fixed-guided beams: (*a*) L, (*b*) t, (c) γ, and (*d*) B

values of other variables to identify the sensitivity of every parameter.

- The larger the L is, the larger the range of negative stiffness is, and moreover, the initial position of buckling, the value of stiffness and the max stress are all inversely proportional to L.
- The effects on the initial position of buckling and the range of negative stiffness by t are more distinct than the value of negative stiffness, whereas t does not have as much varying range as L because of the yield limit.
- It is worth noting that the range of negative stiffness becomes smaller and smaller as the inclined angle decreases, which corresponds to the relationship between the boundary line and the actual displacement curve in Sec. 2.1. When the inclined angle is zero (i.e., the straight beam), the curve will not appear negative stiffness at all.
- In contrast, B has nothing to do with critical buckling positions and ranges, while only making a difference to values of stiffness.

The length and amplifying ratio of the lever are limited by the hinge's deformable stroke. Under the condition that the amplifying ratio meets the design requirements as shown in Fig. 3, the length of the lever should be as small as possible to facilitate miniaturization of the overall size as well.

3.4 Parameters and Theoretical Results. The parameters of AL-7075 are shown in Table 1. The structure parameters as tabulated in Table 2 are under selection to derive a satisfactory output force–displacement performance.

L_i, t_i, and ξ_i ($i = 1, 2, 3, 4$) refer to the length, in-plane width, and initial angle of the fixed-guided beam 1(a), 1(b), 2(a) and 2(b); L_j refers to the length of the jth leverage ($j = 5, 6$); T_k and R_k refer to the in-plane width and the radius of the kth notched circle ($k = 1, 2$); B_f, and B_r refer to the thickness of flexible parts and rigid parts.

Table 1 Material parameters of the proposed TSCFM

Parameter	Value
Density	2830 kg/m^3
Young's modulus	71 GPa
Poisson's ratio	0.33
Tensile yield strength	455 MPa

Then, the analytical results can be obtained as follows. The first-state constant force is 1.24 N ranging from 235.5 to 588.7 μm and the second one is 1.04 N ranging from 902.8 to 1295.2 μm with the standard deviation of 0.02 N.

In addition, the ratios of shuttle mass over beam mass of BBM 1 and BBM 2 are 3.63 and 5.69, respectively, therefore the natural frequency of the first mode is calculated as 356.21 Hz.

4 FEA Simulation Study

4.1 Static Analysis Results

4.1.1 The Static Performances. In this section, the FEA method is used to validate the analytical model of the TSCFM.

Table 2 Structure parameters of the proposed TSCFM

Symbol	Value	Symbol	Value	Symbol	Value
L_1 (mm)	9	t_1 (mm)	0.2	ξ_1 (deg)	1
L_2 (mm)	10	t_2 (mm)	0.2	ξ_2 (deg)	5
L_3 (mm)	22	t_3 (mm)	0.18	ξ_3 (deg)	1.8
L_4 (mm)	22.5	t_4 (mm)	0.2	ξ_4 (deg)	4.5
L_5 (mm)	72	L_6 (mm)	46	B_f (mm)	1
R_1 (mm)	1	R_2 (mm)	1	B_r (mm)	2
T_1 (mm)	0.2	T_2 (mm)	0.2		

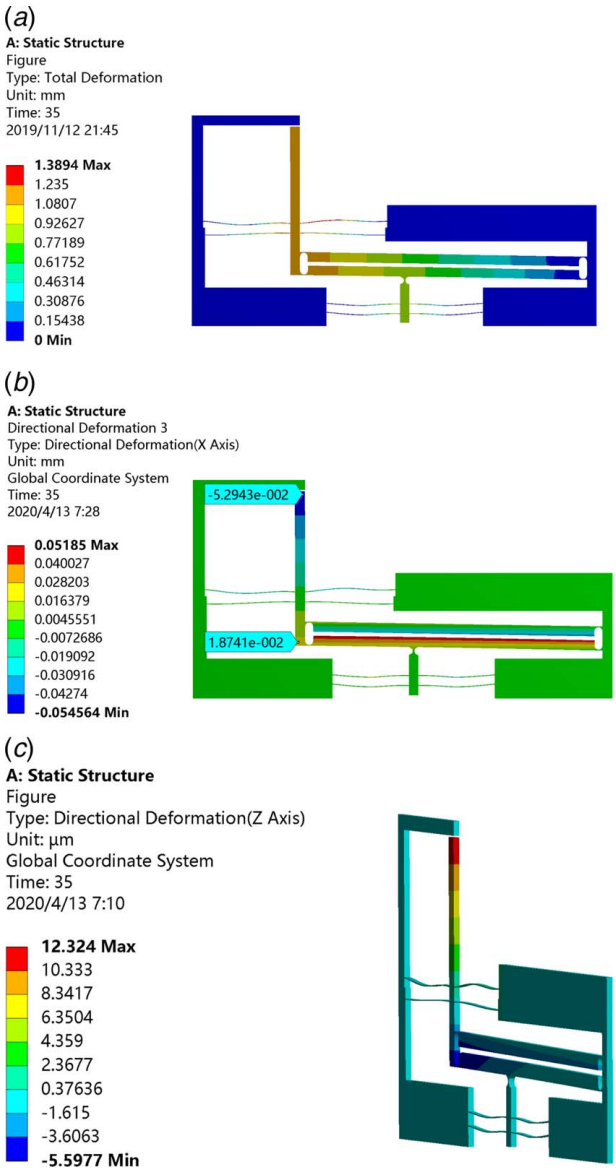

Fig. 12 (*a*) Total deformation nephogram of TSCFM in static structure analysis, (*b*) the in-plane bias of output end, and (*c*) the out-plane deviation

According to the static structure analysis with the option "on" of "large deflection," the amplifying ratio under an input displacement of 0.85 mm is approximately 1.40 as shown in Fig. 12(*a*). The reason why simulation result is smaller than the theoretical one is that the small deformation of leverages and the extension of flexure hinges were ignored in analytical modeling. The in-plane bias and out-plane deviation of the shuttle 2 (output end) are both kept to very small values as shown in Fig. 12(*b*) and Fig. 12(*c*). In addition, the stress performance of TSCFM is conducted to detect whether the stress exceeded the yield strength. The max value of equivalent stress is 223.41 MPa, which indicates that no plastic deformation occurred during the gripping process.

Then, the force–displacement curve of the TSCFM as shown in Fig. 13 can be derived. It is observed that the first-stage constant force is 1.33 N ranging from 150.4 to 456.1 μm and the second one is 1.11 N ranging from 799.9 to 1130.7 μm under FEA simulation. The analytical results are better than FEA ones whose comparison to the former is summarized in Table 3. Apparently, the deviations of constant force performances are caused by one of the amplifying ratio mainly.

4.1.2 The Simulation Comparison With and Without Parasitic Motion. As shown in Fig. 12(*b*), in shuttle 2 (output end) the bias of 0.0019 deg appears due to the comprehensive result of levers' parasitic motion and fixed-guided beams deflection. In order to analyze the influence of asymmetrical deformation of the fixed-guided beams on the output force performance, a simulation without parasitic motion is conducted by applying a frictionless support on the side of shuttle 2. However, the constraint setting forces the flexure hinges to stretch and deviate from the expected stiffness performance. The output force performance of the gripper cannot be used as a comparison term. Therefore, the equivalent stress of an element on the guided end is regarded as a better choice for comparison as shown in Fig. 14.

Compared with Fig. 12(*a*), there is no obvious asymmetry in the fixed-guided beams in Fig. 14(*a*). The displacement amplifying ratio is significantly greater as well. It is observed from Fig. 14(*b*) that the stress variation trend at the guided end is steeper with parasitic motion, making the buckling range smaller. Its value of the stress is larger overall, too. In spite of this, the adverse impact of output performance is pretty small since the angle of bias is only 0.0019 deg.

4.2 Modal Analysis Results. Lastly, the modal analysis is conducted to validate the dynamic model of TSCFM. The natural frequency in the first mode of vibration whose total deformation nephogram is displayed in Fig. 15 is 277.84 Hz under FEA

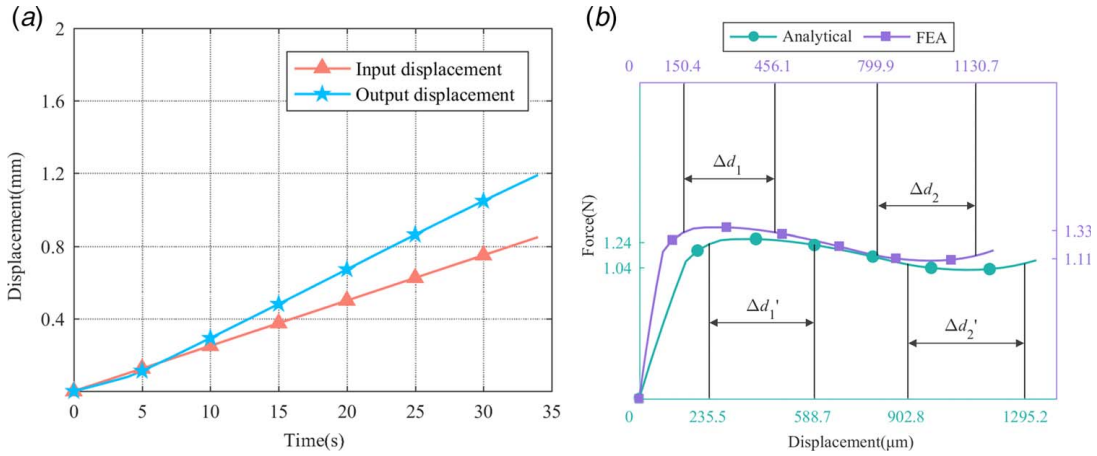

Fig. 13 Performance of TSCFM under FEA simulation: (*a*) relation between input and output displacement and (*b*) Comparison of *F–d* curves under FEA simulation and analytical modeling

Table 3 Comparisons of the analytical and the FEA results

Performance	Analytical	FEA	Deviation
α	1.57	1.40	12.14%
$\triangle d_1$ (μm)	353.2	305.6	15.58%
F_1 (N)	1.24	1.33	6.77%
$\triangle d_2$ (μm)	392.4	330.8	18.62%
F_2 (N)	1.04	1.11	6.31%
f_1 (Hz)	356.21	277.84	28.2%

simulation. It is observed that the warps of BBM 2 and shuttle 2 are the main deforming portion in the first mode. Compared to the FEA results, the analytical one has the deviation of 28.2% whose details are tabulated in Table 3.

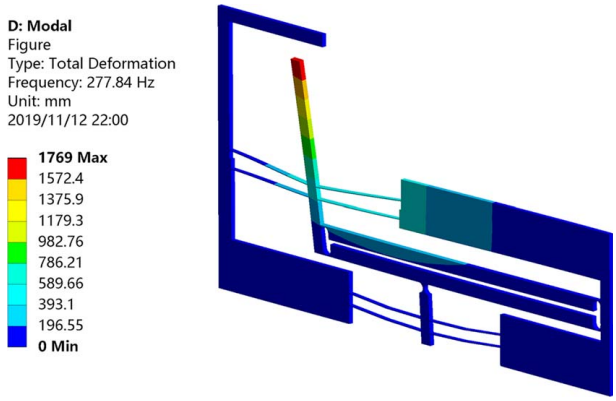

Fig. 15 Total deformation nephogram of the first mode of vibration in modal analysis

5 Discussions

5.1 Comparisons of Modeling Methods. Recently, more research and application of the chain algorithm are being done [45]. For instance, Ma and Chen [46] proposed the beam constraint model (BCM) by splitting a fixed-guided beam into two elements and assembling their equations for the final solution. For ease of comparison, the parameters of the selected fixed-guided beam are shown in Table 4. For the hybrid method we proposed, the BCM and the finite element analysis are all employed respectively to obtain the boundary line of this beam. The comparisons of analytical results and FEA results are tabulated in Table 5, where the boundary positions by BCM are given in Ref. [46] and the boundary positions by our hybrid method are shown in Fig. 16.

Obviously, the chain algorithm can get more accurate analytical results, while the elliptic integral method is still more simple to understand and very useful in stiffness design. Although different loading conditions have great effect on the final result by chain algorithm [1], it can be seen that the chain algorithm has a considerable prospect for modeling method optimization.

5.2 Comparisons of Output Performances. The comparisons of the proposed TSCFM with different designs in Refs. [20–33] are conducted as shown in Table 6. These designs have the following application limitations in the microassembly of multiple parts:

- The constant force of single-stage ones in Refs. [20–26] cannot be adjusted, resulting in the inadaptability to micro assembly with multiple parts and low efficiency.
- Most of the multi-stage constant force mechanisms in Refs. [27–31] are realized by changing preloading displacement or assembly and disassembly of the constant force module. The switching from one constant force to another cannot be carried out continuously in the gripping process. The low operating efficiency, large entire dimension, and poor structural flexibility make it difficult to apply to micro operations.
- A few multi-stage constant force mechanisms in Refs. [32,33] achieve continuous switching by the integrated mechanism design. However, their complex structures increase the overall size and can be hardly applied to microgrippers.

Compared with the above, the proposed TSCFM has the advantages of switching continuity, structural flexibility and integrability, and small entire dimension, which makes it more suitable for efficient microassembly.

6 Conclusions

A novel two-stage constant force microgripper (TSCFM) has been proposed in this paper. First, the parallel connection between multi-stage negative and positive stiffness modules was utilized to mechanism design of TSCFM with the continuous switching of the stages in Fig. 4 for overloading protection of multi-size objects. Second, a hybrid method of EIM and PRBM was applied in modeling and analyzing of TSCFM, which took bistability and nonlinearity of fixed-guided beams as well as linear character and apparent complicacy of flexure hinges into account. Additionally, the parallelogram mechanism played an important role in terms of the amplifying effect of levarages and the stiffness performance of flexure hinges, which not only enabled the initial and final buckling positions of the bistable beams to be arranged at certain spots, but also served as the positive stiffness module to compose the two-stage constant force mechanism.

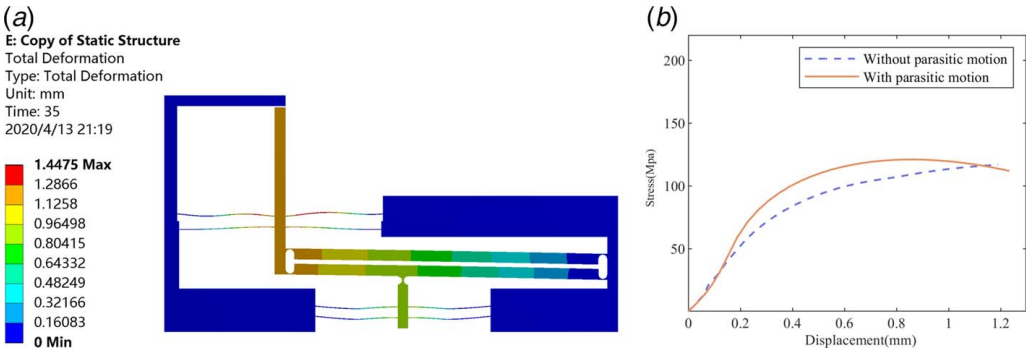

Fig. 14 The simulation comparison with and without parasitic motion: (*a*) total deformation nephogram of TSCFM without parasitic motion and (*b*) the comparison of the equivalent stresses of the guided end

Table 4 Parameters of the fixed-guided beam

Parameter	Value
Young's modulus	1.379 GPa
Length	70 mm
Width	1.5 mm
Thickness	12.55 mm
Initial angle	5.5 deg

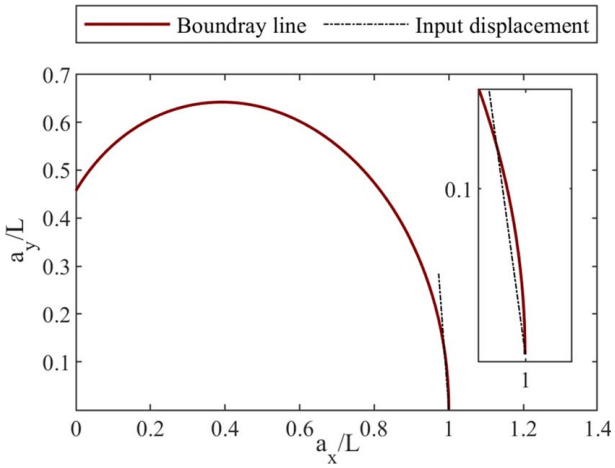

Fig. 16 The boundary line by the hybrid method we proposed

Table 5 Comparisons with the modeling method in Ref. [46]

Performance	Proposed	BCM	FEA
First boundary position (mm)	1.07	1.29	1.42
Second boundary position (mm)	8.83	8.21	8.04

Table 6 Comparisons with different designs in Refs. [20–33]

Designs	a	b	c	d
Refs. [17–23]	×	/	√	/
Refs. [24–28]	√	×	×	Lower
Refs. [29,30]	√	√	×	/
Proposed	√	√	√	Higher

[a]Two/Multi-stage constant force performance.
[b]Switching continuity.
[c]Structural miniaturization.
[d]Efficiency evaluation of multi-object gripping.

This paper provides a novel type of approach to the parallel connection of negative and positive stiffness modules for multi-stage constant force performance, as well as better consistency of the switching of stages during the gripping process. The proposed hybrid method can be used to not only parameter study of synthesis problem of constant force mechanism and general flexure hinges but also the analyses of all compliant mechanisms with both features of distributed and lumped compliance. In the future, the modeling method will be optimized to predict more precisely and topological optimization will be conducted for better static and dynamic performances.

Acknowledgment

This work was supported by China Postdoctoral Science Foundation under Grant No. 2018M642905, National Natural Science Foundation of China under Grant No. 51375349, and Shenzhen Science and Technology Program under No. JCYJ 20170306171514468.

Conflict of Interest

There are no conflicts of interest.

Data Availability Statement

The datasets generated and supporting the findings of this article are obtainable from the corresponding author upon reasonable request. The authors attest that all data for this study are included in the paper.

References

[1] Wang, P., and Xu, Q., 2018, "Design and Modeling of Constant-Force Mechanisms: A Survey," Mech. Mach. Theory, **119**, pp. 1–21.
[2] Verotti, M., Dochshanov, A., and Belfiore, N. P., 2017, "A Comprehensive Survey on Microgrippers Design: Mechanical Structure," ASME J. Mech. Des., **139**(6), p. 060801.
[3] Wu, Z., and Xu, Q., 2018, "Survey on Recent Designs of Compliant Micro-/Nano-Positioning Stages," Actuators, **7**(1), p. 5.
[4] Zhu, B., Zhang, X., Zhang, H., Liang, J., Zang, H., Li, H., and Wang, R., 2020, "Design of Compliant Mechanisms Using Continuum Topology Optimization: A Review," Mech. Mach. Theory, **143**, p. 103622.
[5] Qiu, C., and Dai, J. S., 2020, *Analysis and Synthesis of Compliant Parallel Mechanisms—Screw Theory Approach*, Springer, Cham, Switzerland, pp. 81–98.
[6] McClintock, H., Temel, F. Z., Doshi, N., Koh, J. S., and Wood, R. J., 2018, "The MilliDelta: A High-Bandwidth, High-Precision, Millimeter-Scale Delta Robot," Sci. Rob., **3**(14), p. eaar3018.
[7] Dai, J., 2010, "Surgical Robotics and Its Development and Progress," Robotica, **28**(2), pp. 161–161.
[8] Feng, Z., Liang, W., Ling, J., Xiao, X., Tan, K. K., and Lee, T. H., 2020, "Integral Terminal Sliding-Mode-Based Adaptive Integral Backstepping Control for Precision Motion of a Piezoelectric Ultrasonic Motor," Mech. Syst. Sig. Process., **144**, p. 106856.
[9] Ling, J., Rakotondrabe, M., Feng, Z., Ming, M., and Xiao, X., 2019, "A Robust Resonant Controller for High-Speed Scanning of Nanopositioners: Design and Implementation," IEEE Trans. Control Syst. Technol., **28**(3), pp. 1116–1123.
[10] Zhang, Y., Peng, Y., Sun, Z., and Yu, H., 2018, "A Novel Stick–Slip Piezoelectric Actuator Based on a Triangular Compliant Driving Mechanism," IEEE Trans. Ind. Electron., **66**(7), pp. 5374–5382.
[11] Ming, M., Feng, Z., Ling, J., and Xiao, X., 2020, "Disturbance Observer-Based Model Prediction Control With Real-Time Modified Reference for a Piezo-Actuated Nanopositioning Stage," Trans. Inst. Meas. Control, **42**(4), pp. 813–822.
[12] Liu, S., Dai, J., Li, A., Sun, Z., Feng, S., and Cao, G., 2016, "Analysis of Frequency Characteristics and Sensitivity of Compliant Mechanisms," Chin. J. Mech. Eng., **29**(4), pp. 680–693.
[13] Lobontiu, N., Cullin, M., Petersen, T., Alcazar, J. A., and Noveanu, S., 2013, "Planar Compliances of Symmetric Notch Flexure Hinges: The Right Circularly Corner-Filleted Parabolic Design," IEEE Trans. Autom. Sci. Eng., **11**(1), pp. 169–176.
[14] Kim, H., Kim, J., Ahn, D., and Gweon, D., 2013, "Development of a Nanoprecision 3-DOF Vertical Positioning System With a Flexure Hinge," IEEE Trans. Nanotechnol., **12**(2), pp. 234–245.
[15] Boudaoud, M., and Regnier, S., 2014, "An Overview on Gripping Force Measurement at the Micro and Nano-Scales Using Two-Fingered Microrobotic Systems," Int. J. Adv. Rob. Syst., **11**(3), p. 45.
[16] Chen, W., Qu, J., Chen, W., and Zhang, J., 2017, "A Compliant Dual-Axis Gripper With Integrated Position and Force Sensing," Mechatronics, **47**, pp. 105–115.
[17] Xu, Q., 2018, *Micromachines for Biological Micromanipulation*, Springer, Cham, Switzerland, pp. 145–168.
[18] Komati, B., Clévy, C., and Lutz, P., 2016, "High Bandwidth Microgripper With Integrated Force Sensors and Position Estimation for the Grasp of Multistiffness Microcomponents," IEEE/ASME Trans. Mechatron., **21**(4), pp. 2039–2049.
[19] Liu, Y., Li, D. J., Yu, D. P., Miao, J. G., and Yao, J., 2017, "Design of a Curved Surface Constant Force Mechanism," Mech. Des. Struct. Mach., **45**(2), pp. 160–172.
[20] Liu, Y., Zhang, Y., and Xu, Q., 2017, "Design and Control of a Novel Compliant Constant-Force Gripper Based on Buckled Fixed-Guided Beams," IEEE/ASME Trans. Mechatron., **22**(1), pp. 476–486.
[21] Zhang, X., and Xu, Q., 2019, "Design and Analysis of a 2-dof Compliant Gripper With Constant-Force Flexure Mechanism," J. Micro-Bio Rob., **15**(1), pp. 31–42.

[22] Liu, Y., and Xu, Q., 2016, "Design and Analysis of a Micro-gripper with Constant Force Mechanism," 2016 12th World Congress on Intelligent Control and Automation (WCICA), Guilin, China, June 12–15, pp. 2142–2147.
[23] Liu, Y., and Xu, Q., 2016, "Design of a Compliant Constant Force Gripper Mechanism Based on Buckled Fixed-Guided Beam," 2016 International Conference on Manipulation, Automation and Robotics at Small Scales (MARSS), Paris, France, July 18–22, pp. 1–6.
[24] Wang, J. Y., and Lan, C. C., 2014, "A Constant-Force Compliant Gripper for Handling Objects of Various Sizes," ASME J. Mech. Des., **136**(7), p. 071008.
[25] Wang, D. A., and Chen, J. H., 2013, "A Constant-Force Bistable Micromechanism," Sens. Actuators, A: Phys., **189**, pp. 481–487.
[26] Lan, C. C., Wang, J. H., and Chen, Y. H., 2010, "A Compliant Constant-Force Mechanism for Adaptive Robot End-Effector Operations," 2010 IEEE International Conference on Robotics and Automation, Anchorage, AK, May 3–7, pp. 2131–2136.
[27] Chen, Y. H., and Lan, C. C., 2012, "An Adjustable Constant-Force Mechanism for Adaptive End-Effector Operations," ASME J. Mech. Des., **134**(3), p. 031005.
[28] Kuo, Y. L., Huang, S. Y., and Lan, C. C., 2019, "Sensorless Force Control of Automated Grinding/Deburring Using An Adjustable Force Regulation Mechanism," 2019 International Conference on Robotics and Automation (ICRA), Montreal, QC, Canada, May 20–24, pp. 9489–9495.
[29] Hao, G., Mullins, J., and Cronin, K., 2017, "Simplified Modelling and Development of a Bi-Directionally Adjustable Constant-Force Compliant Gripper," Proc. Inst. Mech. Eng., Part C: J. Mech. Eng. Sci., **231**(11), pp. 2110–2123.
[30] Chen, C. C., and Lan, C. C., 2017, "An Accurate Force Regulation Mechanism for High-Speed Handling of Fragile Objects Using Pneumatic Grippers," IEEE Trans. Autom. Sci. Eng., **15**(4), pp. 1600–1608.
[31] Zhang, X., Wang, G., and Xu, Q., 2018, "Design, Analysis and Testing of a New Compliant Compound Constant-Force Mechanism," Actuators, **7**(4), p. 65.
[32] Hu, J., and Chen, X., 2018, "Optimized Design of A Micro-motion Stage With Zero Stiffness," Opt. Precis. Eng., **26**(6), pp. 1430–1440.
[33] Xu, Q., 2017, "Design of a Large-Stroke Bistable Mechanism for the Application in Constant-Force Micropositioning Stage," ASME J. Mech. Rob., **9**(1), p. 011006.
[34] Chen, G., and Ma, F., 2015, "Kinetostatic Modeling of Fully Compliant Bistable Mechanisms Using Timoshenko Beam Constraint Model," ASME J. Mech. Des., **137**(2), p. 022301.
[35] Ma, F., and Chen, G., 2016, "Modeling Large Planar Deflections of Flexible Beams in Compliant Mechanisms Using Chained Beam-Constraint-model," ASME J. Mech. Rob., **8**(2), p. 021018.
[36] Ling, M., Howell, L. L., Cao, J., and Jiang, Z., 2018, "A Pseudo-Static Model for Dynamic Analysis on Frequency Domain of Distributed Compliant Mechanisms," ASME J. Mech. Rob., **10**(5), p. 051011.
[37] Ling, M., Cao, J., Howell, L. L., and Zeng, M., 2018, "Kinetostatic Modeling of Complex Compliant Mechanisms With Serial-Parallel Substructures: A Semi-Analytical Matrix Displacement Method," Mech. Mach. Theory, **125**, pp. 169–184.
[38] Qiu, C., Qi, P., Liu, H., Althoefer, K., and Dai, J. S., 2016, "Six-Dimensional Compliance Analysis and Validation of Orthoplanar Springs," ASME J. Mech. Des., **138**(4), p. 042301.
[39] Yu, Y. Q., Howell, L. L., Lusk, C., Yue, Y., and He, M. G., 2005, "Dynamic Modeling of Compliant Mechanisms Based on the Pseudo-Rigid-body Model," ASME J. Mech. Des., **127**(4), pp. 760–765.
[40] Venkiteswaran, V. K., and Su, H. J., 2016, "Extension Effects in Compliant Joints and Pseudo-Rigid-Body Models," ASME J. Mech. Des., **138**(9), p. 092302.
[41] Jin, M., Yang, Z., Ynchausti, C., Zhu, B., Zhang, X., and Howell, L. L., 2020, "Large Deflection Analysis of General Beams in Contact-Aided Compliant Mechanisms Using Chained Pseudo-Rigid-Body Model," ASME J. Mech. Rob., **12**(3), p. 031005.
[42] Holst, G. L., Teichert, G. H., and Jensen, B. D., 2011, "Modeling and Experiments of Buckling Modes and Deflection of Fixed-Guided Beams in Compliant Mechanisms," ASME J. Mech. Des., **133**(5), p. 051002.
[43] Zhang, A., and Chen, G., 2013, "A Comprehensive Elliptic Integral Solution to the Large Deflection Problems of Thin Beams in Compliant Mechanisms," ASME J. Mech. Rob., **5**(2), p. 021006.
[44] Nejad, M. Z., Hadi, A., and Rastgoo, A., 2016, "Buckling Analysis of Arbitrary Two-Directional Functionally Graded Euler–Bernoulli Nano-Beams Based on Nonlocal Elasticity Theory," Int. J. Eng. Sci., **103**, pp. 1–10.
[45] Ling, M., Howell, L. L., Cao, J., and Chen, G., 2020, "Kinetostatic and Dynamic Modeling of Flexure-Based Compliant Mechanisms: A Survey," ASME Appl. Mech. Rev., **72**(3), p. 030802.
[46] Ma, F., and Chen, G., 2016, "Bi-BCM: A Closed-Form Solution for Fixed-Guided Beams in Compliant Mechanisms," ASME J. Mech. Rob., **9**(1), p. 014501.